

## Monitoring Anomalies in 3D Bioprinting with Deep Neural Networks

Zeqing Jin, Zhizhou Zhang, Xianlin Shao, and Grace X. Gu\*

Cite This: <https://doi.org/10.1021/acsbomaterials.0c01761>

Read Online

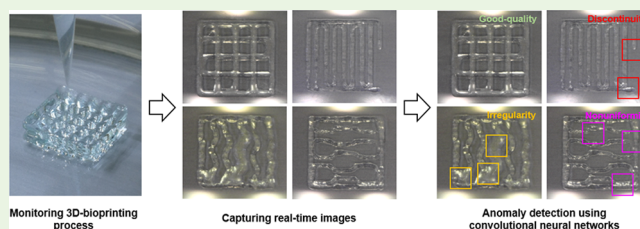
ACCESS |

Metrics &amp; More

Article Recommendations

**ABSTRACT:** Additive manufacturing technologies have progressed in the past decades, especially when used to print biofunctional structures such as scaffolds and vessels with living cells for tissue engineering applications. Part quality and reliability are essential to maintaining the biocompatibility and structural integrity needed for engineered tissue constructs. As a result, it is critical to detect for any anomalies that may occur in the 3D-bioprinting process that can cause a mismatch between the desired designs and printed shapes. However, challenges exist in detecting the imperfections within oftentimes transparent bioprinted and complex printing features accurately and efficiently. In this study, an anomaly detection system based on layer-by-layer sensor images and machine learning algorithms is developed to distinguish and classify imperfections for transparent hydrogel-based bioprinted materials. High anomaly detection accuracy is obtained by utilizing convolutional neural network methods as well as advanced image processing and augmentation techniques on extracted small image patches. Along with the prediction of various anomalies, the category of infill pattern and location information on the image patches can be accurately determined. It is envisioned that using our detection system to categorize and localize printing anomalies, real-time autonomous correction of process parameters can be realized to achieve high-quality tissue constructs in 3D-bioprinting processes.

**KEYWORDS:** additive manufacturing, 3D bioprinting, computer vision, machine learning, convolutional neural networks



## 1. INTRODUCTION

Additive manufacturing, otherwise well-known as 3D printing, has been widely applied to various fields including the aerospace industry, biological engineering, and autonomous vehicles.<sup>1–6</sup> Recent advances in tissue engineering have realized 3D bioprinting of biological components such as living tissues and human organs.<sup>7–9</sup> 3D bioprinting is now actively applied to create biocompatible materials and structures for functional living cells. Among the bioprinted materials, hydrogels are one of the most widely applied materials for their cross-linking capability to create scaffold structures for tissue engineering applications.<sup>10,11</sup> For biological constructs such as tissues, it is critical to obtain a high-quality print as close to the desired design as possible to ensure robust functionality. However, unlike typical 3D-printing methods using polymers or metal powder, the challenge of achieving high-quality prints during the 3D-bioprinting process lies in understanding the rheological property of the hydrogels as they are sensitive to the additive concentration (e.g., methylcellulose, alginate) as well as the choice of printing parameters during fabrication.<sup>12</sup> For example, studies have shown a catastrophic failure of bioprinted parts such as the collapse of filament<sup>13</sup> and broken lines<sup>14</sup> due to suboptimal printing parameters. Hence, numerous studies have explored the effects of printing parameters on part quality. He et al. analyzed the impact of printing factors including extrusion pressure, feed rate, printing distance on the printing quality of

hydrogel such as dimensional accuracy, and printability.<sup>14</sup> Naghieh et al. focused on the influence of hydrogel composition and printing parameters on the printability of scaffolds. Dimensional accuracy including pore size and strand diameter as well as printing irregularity are explored in the study.<sup>15</sup> Anomalies including discontinuous printing rasters, improper line width, and bubbles are commonly seen in the printing process.<sup>16,17</sup> While research has been actively conducted on identifying these anomalies, challenges still lie in the efficiency and accuracy of the assessment process. The current anomaly evaluation process faces challenges when it comes to efficiency and accuracy; it requires heavy postprocessing analysis after the print is finished and largely relies on the experience of the operator, thereby causing wasted materials and delaying the discovery of anomalies.

In this paper, an anomaly detection system is established to recognize and distinguish anomalies accurately and efficiently in a layer-by-layer configuration for bioprinted materials. Three major anomalies including discontinuity (broken raster), nonuniformity (unsmoothed surface), and irregularity (im-

**Special Issue:** Engineering Bioinspired and Biological Materials

**Received:** December 19, 2020

**Accepted:** April 13, 2021

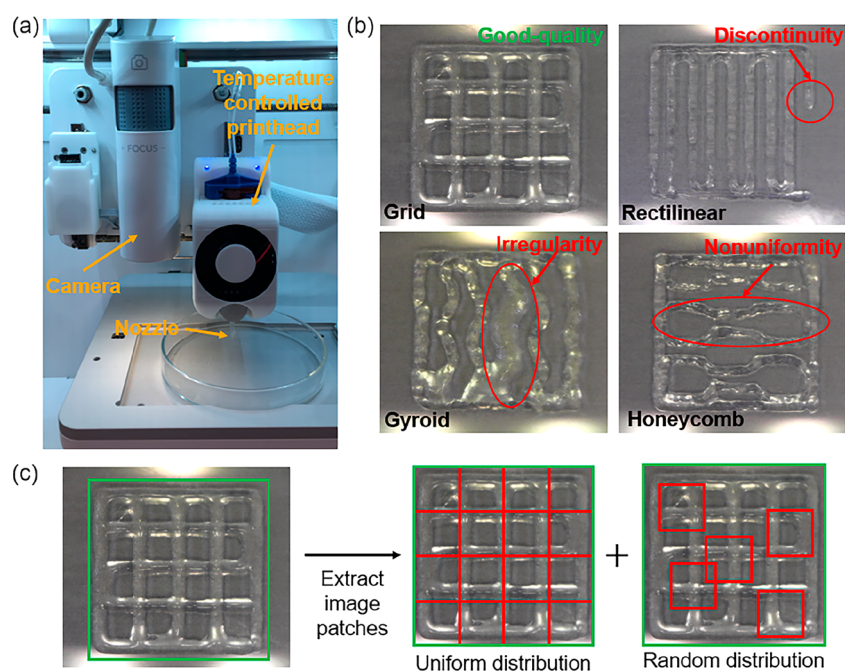


**Figure 1.** (a) Experimental setup of the anomaly detection system for a 3D-bioprinting platform. (b) Raw image data showing four different infill pattern examples and three anomaly cases. (c) An illustration visualizing the image processing procedure. The area of interest shown in the green bounding box is first determined and cropped into an  $800 \times 800$  pixels size. Smaller image patches (input images) are then extracted uniformly and randomly.

proper line width) are explored for the first layer of the print which is considered the important foundation of the entire print. Due to the transparent and complex features of these anomalies, machine learning methods are actively incorporated for this problem to explore and distinguish the underlying hidden patterns behind real-time printing images. Recently, machine learning methods have progressed dramatically in terms of efficiency and have seen promising applications in predictive materials modeling, advanced manufacturing, autonomous vehicles, and biomechanics, among many others.<sup>18–24</sup> Specifically, two baseline models as well as two advanced convolutional neural network (CNN) models are implemented using our collected and processed image data set. Evaluation metrics are analyzed on the training results as well as testing data set to validate and compare the performance of each model. Moreover, studies are further focused on analyzing a single anomaly and a specific infill pattern using evaluation factors and visualization methods. Additionally, discussions are conducted on the impact of printing parameters on printing quality and methods to find the optimal combination of printing parameters. Our work has the following contributions: 1) development of an anomaly detection system for bioprinting in a layer-wise configuration; 2) realization of an efficient and accurate anomaly detection model based on machine learning methods; and 3) demonstration of applying machine learning methods to transparent object detection. The paper is organized as follows. Section 2 discusses the process of image data collection, the methods utilized for classification models, and metrics used for results evaluation. Section 3 shows, compares, and visualizes the training results as well as the performance from the perspective of an overall anomaly, individual anomaly, and anomalies in different infill patterns. The effects of printing parameters on printing quality and corresponding optimizing methods are also discussed. Section

4 summarizes and concludes the work and proposes future perspectives.

## 2. MATERIALS AND METHODS

In this section, the experimental setup and the preparation of the image data set of this study used to train our machine learning models will be illustrated in detail. Moreover, four anomaly classification models as well as corresponding evaluation metrics are introduced.

**Experimental Setup and Image Data Preparation.** In this paper, an extrusion-based bioprinter using an air pressure (pneumatic dispensing) method is conducted through CELLINK BIO X and GelMA A (gelatin methacrylate and alginate) material.<sup>25,26</sup> During the printing process, a temperature-controlled printhead is equipped to adjust and maintain the required printing temperature needed for the material. The printing temperature of GelMA A is set to  $26^\circ\text{C}$  in the experiments. At the side of the printhead, a camera is mounted on the moving platform and captures an image after each printing layer is finished. A detailed display of the experimental setup is shown in Figure 1(a). As the quality of the first layer is rather significant and determines the foundation of the final print as mentioned in the Introduction section, the full image of the first layers is captured and recorded as raw data. By manually adjusting the extrusion pressure and printing speed, a total of 240 raw images of data are collected with three anomalies (discontinuity, irregularity, and nonuniformity) under four different infill patterns including grid, rectilinear, gyroid, and honeycomb (with each pattern having 60 raw images) (Figure 1(b)). The determination of the data set size involves two aspects. First, the collected data set needs to cover all the different combinations of three anomalies under varying extents. Second, the size of the data set is chosen to balance the amount of labeling work and achieving a satisfying anomaly detection performance. Additionally, the adjusting range of extrusion pressure and printing speed is 10–20 kPa and 3–8 mm/s, respectively. It is worth noting that different anomalies can occur due to the unexpected clogging of the print nozzle caused by temperature variation even under the same printing parameters. From the experimental setup, the main body of the hydrogel cartridge is kept in the temperature-controlled printhead, whereas the nozzle is exposed to the environment. Hence, the labeling

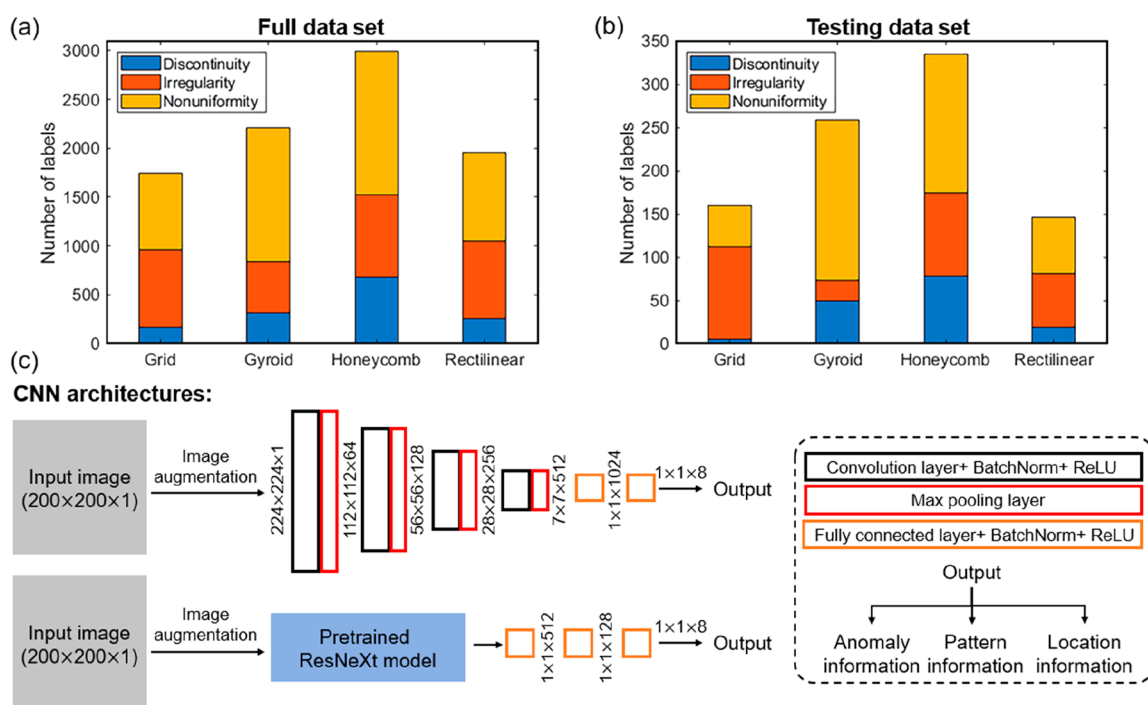


**Figure 2.** (a,b) Bar charts summarizing detailed anomaly information for both full and testing data sets. The number of labels for three types of anomalies under four infill patterns is counted. (c) Flow diagram showing the architectures of applied CNN models. The self-designed CNN architecture is illustrated at the top, and the pretrained model is shown at the bottom. Image size information is displayed in the vertical direction, and legends are marked in the bounding box with a dashed line.

process will be based on the features of the actual prints instead of direct mapping from the process parameters. Specifically, image patches with good printing quality will be first labeled as benchmarks. After that, anomalies such as thinner or thicker rasters are labeled as irregularity, and unsmoothed surfaces are labeled as nonuniformity. The labeling process will be performed by one operator to minimize the noise in the labeling process. The process parameters are adjusted randomly in the given range to create different extents of various anomalies. In general, increasing printing speed tends to generate discontinuity, while irregularity and nonuniformity are likely to occur under higher extrusion pressure. The raw image data is further cropped into an  $800 \times 800$  pixels square image with the location of interest shown in the green bounding box of Figure 1(c). For each pattern, the processed images are randomly selected into training, validation, and testing data sets under the ratio of 7:2:1. Hence, the number of images in each data set is 42, 12, and 6 correspondingly. In order to locate the anomalies more accurately, 16 smaller image patches ( $200 \times 200$  pixels) are extracted uniformly in spatial distribution, as well as another 16 patches are obtained randomly within the processed image. The size of image patches is larger than the grid size of the grid pattern to avoid selecting blank images. It is worth noting that smaller image patches yield a higher resolution when it comes to anomaly detection, but at the same time, the labeling work on the image data preparation process is increased. Hence, the size of the small image patches is chosen to balance both infill pattern complexity and labeling difficulty. The extracted patches are regarded as input images of the machine learning model and are further labeled using the one-hot encoding method with anomaly information (3 elements), location information (4 elements), and location information (whether the perimeter is inside the patches, 1 element). For example, anomaly information “110” indicates the batch image has both discontinuity and irregularity anomaly, following with location information “1000” standing for the grid infill pattern, and the last element ‘1’ means the perimeter is in the image. If such conditions are not fulfilled, the element is then labeled as ‘0’. The location information is included to distinguish the condition that an infill raster is tied parallel together with the

perimeter from an irregularity anomaly. Lastly, Figure 2(a,b) summarizes the detailed anomaly information on the full data set and testing data set, presenting the number of labels for each anomaly under four infill patterns.

**Anomaly Classification Models.** In this section, four models are evaluated on the anomaly classification problem. The first one is a constant predictor that establishes the difficulty of the task and provides the performance that the rest of the models must exceed. The second model is a linear support vector machine (SVM) classifier that decides whether each individual defect is present in the image patch. The SVM model is trained on the histogram of oriented gradients (HoG) features<sup>27</sup> extracted from the images; the HoG is chosen for its competitive (pre-CNN) performance on large-scale image recognition data sets.<sup>28</sup> The SVM model offers a strong baseline that motivates the use of modern convolutional neural network (CNN) models. The architectures of the applied CNN models are shown in Figure 2(c). Specifically, the third model is a self-designed four-layer CNN network to verify the performance of a shallow network on this problem. Lastly, the fourth model is a ResNeXt-50,<sup>29</sup> the largest variant of which has obtained state-of-the-art results on ImageNet.<sup>30</sup> However, given the rather small size of the bioprinting data set, this model uses the final layer of a pretrained ResNeXt-50 as a static feature extractor that feeds into a small, optimized multilayer perceptron as shown in Figure 2(c); despite ImageNet images being full-color and of natural scenes, the low-level pretrained feature detectors are still applicable.<sup>31</sup> The neural network models are trained to predict the defect logits (anomaly information), the printout’s pattern (e.g., grid, honeycomb, pattern information), and whether the image patch is viewing the interior or exterior of the print (location information). The objectives jointly use the Adam<sup>32</sup> optimizer in a multitask setup<sup>33</sup> to regularize the model in the present small-data regime. To further decrease the possibility of overfitting, in each epoch, an image patch is resized to 256 pixels, randomly cropped to 224, and randomly flipped; more advanced data augmentation strategies like color jitter and rotation are not applied since they do not match transformations that would be seen in test data. Moreover, the output of the model is further decomposed and standardized into

Table 1. Performance Summary of the Classification Models

data set	model	method	anomaly accuracy	anomaly precision	anomaly recall	anomaly F1-score
validation	baseline 1	constant	0.677	0.598	0.514	0.553
validation	baseline 2	SVM	0.745	0.724	0.553	0.627
validation	CNN	self-designed	0.847	0.813	0.794	0.801
validation	CNN	pretrained	0.878	0.851	0.843	0.955
testing	baseline 1	constant	0.676	0.598	0.512	0.552
testing	baseline 2	SVM	0.759	0.752	0.556	0.646
testing	CNN	self-designed	0.874	0.847	0.826	0.836
testing	CNN	pretrained	0.901	0.902	0.836	0.868

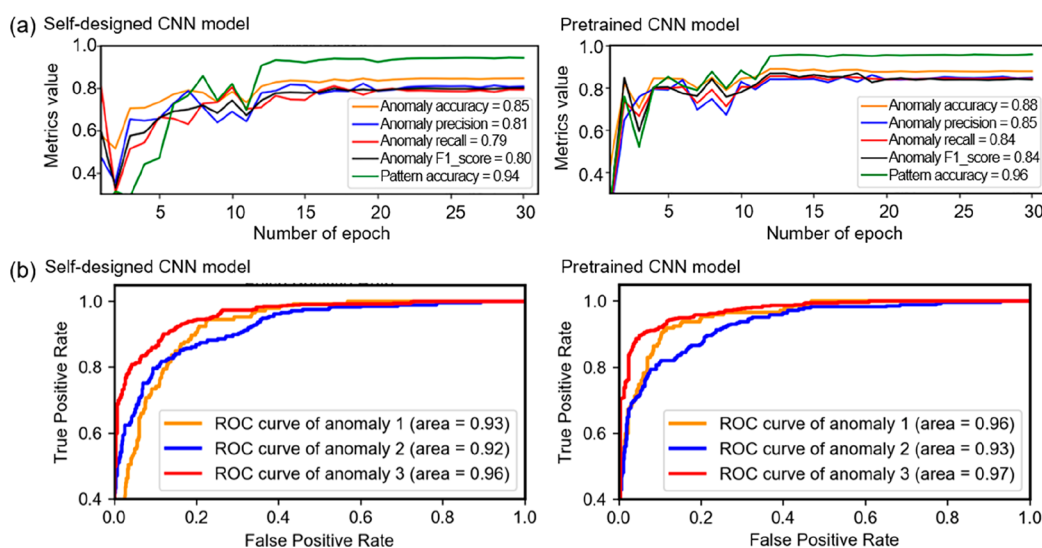


Figure 3. (a) The performance of the applied CNN model within 30 epochs of training on the validation data set. (b) The ROC curves of every single anomaly on the testing data set.

three parts. Specifically, both anomaly information and location information outputs are processed using a sigmoid function to standardize the values between 0 and 1 since the information is in a binary case setting. Pattern information output is regulated through the log-softmax function (log operation after the softmax function) from the probability point of view. In the training process, the total loss function is composed of anomaly loss, pattern loss, and location loss together with three regularization coefficients (1, 0.1, and 0.1, respectively) attached to each loss. Both anomaly loss and location loss are calculated using the binary cross-entropy (BCE) loss function which gives output at each element position range from 0 to 1. For a predicted value larger than 0.5, it can be interpreted as true (detecting specific anomaly or perimeters) in this element. Pattern loss is obtained through the negative log-likelihood (NLL) loss function, where the sum of the output is 1, and the position of the largest element indicates the category of the infill pattern.<sup>34,35</sup> Last but not least, the three regularization coefficients are specifically designed to balance the performance of the overall prediction while maintaining the main objective of anomaly classification.

**Evaluation Metrics.** The performance of the model is evaluated through the following aspects. First and foremost, the accuracy, precision, recall, and F1-score of the anomaly detection are analyzed. In order to determine these values, four additional terms are defined. For a single prediction, true positive (TP) and true negative (TN) stand for the label and prediction both being equal to 1 or 0, respectively; false positive (FP) and false negative (FN) describe an opposite prediction on the label 0 and 1, respectively. These four terms sum up the entire evaluation data set. Hence, the evaluation terms can be expressed in the equations as follows:

$$\text{Accuracy} = \frac{\text{TP} + \text{TN}}{\text{TP} + \text{TN} + \text{FP} + \text{FN}} \quad (1)$$

$$\text{Precision} = \frac{\text{TP}}{\text{TP} + \text{FP}}, \quad \text{Recall} = \frac{\text{TP}}{\text{TP} + \text{FN}} \quad (2)$$

$$\text{F1-score} = \frac{2 \cdot \text{Precision} \cdot \text{Recall}}{\text{Precision} + \text{Recall}} \quad (3)$$

Besides the evaluation of anomalies, accuracy is also calculated on pattern and location predictions. Since pattern and location information are not the major concern in the anomaly detection problem, the analysis in the next **Results and Discussion** section focuses on the performance of the anomaly classification task.

### 3. RESULTS AND DISCUSSION

**Performance of the Classification Models on Overall Anomaly Cases.** The results of the applied models in both validation and testing data sets are summarized and presented in Table 1. In addition, Figure 3(a) shows the performance of the CNN models on the validation data set against the number of training epochs. Note, the evaluation metrics shown in the table and figure are the average value of the three anomaly cases. By viewing the accuracy and F1-score of the anomaly prediction, both CNN models perform better than the baseline models in both validation and testing data sets. Here, the F1-score is the operation of precision and recall, which indicates the robustness of a model on the prediction of both true and false labels. The results further demonstrate the necessity and feasibility of applying CNN methods to this problem. In terms of the two CNN models, the performance of the self-designed four-layer CNN architecture is competitive against the pretrained one. It implies that this four-layer CNN network is comparably sufficient to extract the anomaly features hidden

**Table 2. Performance Summary of the Predictions of a Single Anomaly on the Testing Data Set**

method	anomaly category	anomaly accuracy	anomaly precision	anomaly recall	anomaly F1-score	pattern accuracy	location accuracy
self-designed	anomaly 1	0.878	0.680	0.680	0.680	0.969	0.913
self-designed	anomaly 2	0.861	0.814	0.817	0.816		
self-designed	anomaly 3	0.884	0.924	0.878	0.901		
pretrained	anomaly 1	0.915	0.836	0.694	0.758	0.974	0.922
pretrained	anomaly 2	0.872	0.858	0.793	0.824		
pretrained	anomaly 3	0.915	0.948	0.908	0.928		

**Table 3. Performance Summary of the Predictions of Different Infill Patterns on the Testing Data Set**

method	infill pattern	anomaly accuracy	anomaly precision	anomaly recall	anomaly F1-score	pattern accuracy	location accuracy
self-designed	grid	0.872	0.801	0.699	0.747	0.969	0.906
self-designed	honeycomb	0.852	0.861	0.890	0.875	0.958	0.885
self-designed	rectilinear	0.915	0.813	0.863	0.837	0.984	0.917
self-designed	gyroid	0.858	0.873	0.799	0.835	0.964	0.943
pretrained	grid	0.865	0.800	0.667	0.727	0.969	0.906
pretrained	honeycomb	0.896	0.920	0.899	0.909	0.964	0.911
pretrained	rectilinear	0.939	0.888	0.870	0.879	0.990	0.927
pretrained	gyroid	0.905	0.943	0.838	0.888	0.974	0.943

behind the images. Moreover, the pretrained CNN network achieves the best performance among the four models. On the one hand, the pretrained feature extractor can be a general and helpful tool even if there are huge distinctions between our data set and ImageNet. On the other hand, a deeper network shows a better result for our problem. However, the elevation on the performance slows down and reaches a limit with an increased number of layers. One additional remark we would like to add is the choice of model output size and loss function. In the first place, we only predict the anomaly information, and hence, the output size of the model only has three elements. The performance of the pretrained model on the anomaly detection task only reaches an overall accuracy of 0.82 and F1-score of 0.80. This is an interesting finding as the additional pattern and location labels are informative and help regularize the detection of anomalies. Moreover, it also implies that the features between the interior and exterior of the bioprinted part are distinct to each other and their quality assessment can be treated differently to improve model accuracy. Additionally, more complicated printing patterns such as vascularized tissue constructs can be evaluated through the extracted small image patches.

**Performance of the Classification Models on Single Anomaly Cases.** Besides the evaluation of the overall performance of the anomaly prediction, analysis is focused on the performance of every single anomaly. The receiver operating characteristic (ROC) curve is performed on the testing data set of every single anomaly. The ROC curve is the plot of the true positive rate (recall) against the false positive rate (FN over the sum of FN and TP), and the area under the curve (AUC) illustrates the capability of a binary classifier model. The AUC value of a perfect classifier is 1.0, and the AUC value of a random classifier is 0.5. Figure 3(b) shows the ROC curves of three individual anomalies for both CNN models. The AUC values achieve around 0.95 for all the cases and indicate a satisfying performance of the classifier. In addition, a detailed summary of the evaluation metrics on each anomaly as well as pattern and location information predictions are shown in Table 2. Here, anomalies 1, 2, and 3 stand for discontinuity, irregularity, and nonuniformity anomalies, respectively, for both Figure 3(b) and Table 2.

For anomaly detection orientated applications, both accuracy and recall are key factors of the performance of the model. The former parameter shows the overall correctness of the entire data set, while the latter one reflects the accuracy among the images having anomalies (true labels). For the three anomalies, while discontinuity is believed to be one of the most obvious defects based on human visual inspection, it has the lowest recall value among all three anomalies. The inferior performance on discontinuity is believed to be caused by the small and isolated feature of the anomaly. Unlike the other two anomalies which have a raster or several rasters of defects, the feature of discontinuity is subtle and regional where the characteristic information is likely to be lost in the calculation and propagation of the machine learning model. It can be seen that the predictions on the irregularity anomaly perform moderately in recall value and worst in accuracy. As the feature of this anomaly involves thin or thick rasters (from the top view), it poses many difficulties during the labeling process for an experienced user. Moreover, the distinction between the infill raster tying parallel together with the perimeter and irregularity anomaly requires prior design information on the print. Last but not least, nonuniformity is thought to be the hardest anomaly to classify, as the unsmooth surface is difficult to detect from the top view. However, the results for the nonuniformity anomaly detection are the best in terms of all the evaluation metrics (accuracy, precision, recall, and F1-score) among all three anomalies.

**Performance of the Classification Models on Different Infill Patterns.** After analyzing the performance on single anomaly cases, viewing the prediction results with respect to different infill patterns is also another important point of view. A detailed summary of the performance of the testing data set is shown in Table 3. Based on the result of the F1-score, we can conclude that the honeycomb infill pattern achieves the best performance on anomaly classification, and the rectilinear pattern obtains superior results on pattern recognition. The gyroid pattern shows the highest accuracy on location information prediction. Although the honeycomb infill pattern is believed to be the most complicated case based on its features and winding printing path, the performance shows an opposite result compared to our initial thoughts. This may

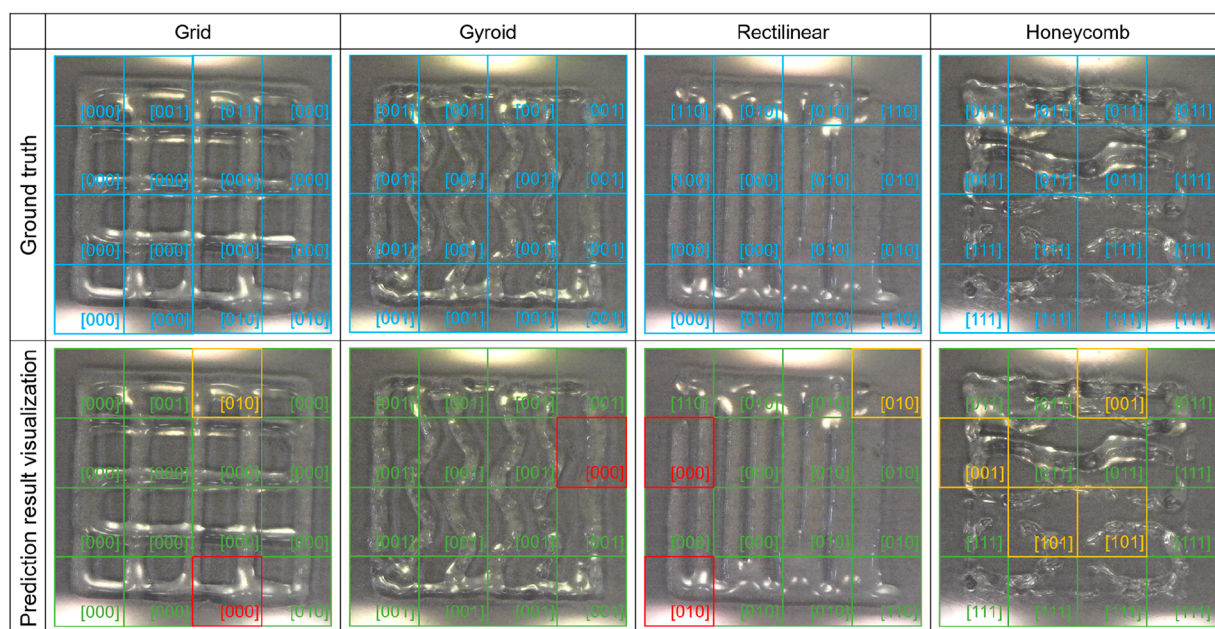


**Figure 4.** Anomaly prediction result visualization on sample images of the testing data set. Ground truth images are marked in blue, and prediction images are presented using green (all anomalies are detected), yellow (partial anomalies are correctly detected), and red (all anomalies are not detected or wrongly predicted) colors for bounding boxes and labels.

imply that the complex feature of the honeycomb infill pattern has a diverse contrast against the other three infill patterns, and hence, it is easier for the machine learning model to learn the distinct information behind this unique pattern.

**Results Visualization and Discussion on Optimizing Printing Parameters.** To better present the prediction on anomalies in different infill patterns, prediction results are visualized using different colors on the sample images of the testing data set (Figure 4). In Figure 4, discontinuity is correctly predicted in the honeycomb pattern (the last second column), while it failed in the rectilinear one (the second last column). The feature extractor may fail if the anomaly (breaking position in this case) is near the edge of the image. In terms of irregularity anomalies, based on Figure 4, thin irregularity anomalies in both grid and rectilinear patterns are not predicted correctly (shown in red bounding boxes). However, thick irregularity anomalies in rectilinear patterns are all correctly predicted. This may be caused by the imbalanced training data set as a thicker irregularity is more common (more images in the collected data set) due to the suboptimal printing temperature settings. Lastly, for the nonuniformity anomaly, it only fails for one image of the gyroid pattern and succeeds with all other predictions. It is believed that both the unsmooth stripe features and reflection of the surface light help with the recognition of the nonuniformity anomaly.

As mentioned in the [Experimental Setup and Image Data Preparation](#) section, the occurrence of anomalies is highly related to the setting of printing parameters including extrusion pressure, printing speed, printhead temperature, printing bed temperature, and humidity of the environment. A higher extrusion pressure results in extruding too much material in a unit time and could lead to irregularity anomaly. The choices of printing speed and printhead temperature are related to the rheological property of the printing material, where improper settings such as an increased printing speed could cause discontinuity or a higher printhead temperature will decrease the viscosity of the hydrogels and give rise to an irregularity

anomaly. Hence, systematic optimization methods such as design of experiments (DOE) can be applied in future studies to find the best combinations of the printing parameters. Moreover, as the quality of the prints is usually correlated with multiple printing parameters, machine learning methods including principal component analysis (PCA) can be used to determine the dominant printing parameters. The bioprinter has a quick response to the change of printing speed, while a longer latency time to the modification of temperature. Standard patterns such as multiple lines of raster or continuous spiral circle can be printed using an increasing printing speed under different sets of printhead and print bed temperature. Based on the features of the print, an optimal set of printing parameters can be preliminarily determined. Due to the complex geometry of the prints, further adjustments on preflow and postflow time may be needed for better printing quality. Additionally, the radius of curvature (ROC) of the geometry can also affect the occurrence of anomalies. For example, decreasing the printing speed at sharp corners can effectively avoid discontinuity. Quantitative analysis can be further conducted to find the relationship between proper printing parameters against geometrical features (e.g., ROC) in both 2D and 3D configurations. The results are believed to be helpful for fine-tuning the process parameters when printing with complex geometries. In this study, a good-quality first-layer process parameter setting is shown in Table 4. Moreover, an environment with elevated humidity would generate moisture at the surface of the printing plate and easily induce nonuniformity anomaly. Hence, a constant dry environment

**Table 4.** Set of Printing Parameters That Can Print a Good-Quality First Layer in the Experiments

printing parameters	nozzle diameter	extrusion pressure	printing speed	print bed temperature	preflow time
value	0.2 mm	12 kPa	5 mm/s	13 °C	350 ms

within the bioprinter is essential to achieve a stable printing process.

#### 4. CONCLUSIONS

In summary, the established anomaly system and developed machine learning method are able to successfully detect and recognize the type of different anomalies in a layer-by-layer configuration for bioprinted materials. The best CNN model reaches an overall accuracy of 0.901 and F1-score of 0.955 on the testing and validation data sets, respectively. Among all three anomalies, nonuniformity detection reaches the best performance, while discontinuity performs the worst. It is believed that the results can be further improved by improving the balance of different anomalies within the data set and fixing the environment's conditions (e.g., lighting) during the data collection. It is hypothesized that dyeing the material with colors can be helpful for this problem. However, mixing the extra additive (food coloring) could potentially change the printability of the material and requires further tuning of the printing parameters. Additionally, transfer learning can also be applied to this problem in the future to minimize the manual labeling process and enhance its general application capability.

#### AUTHOR INFORMATION

##### Corresponding Author

Grace X. Gu – Department of Mechanical Engineering,  
University of California, Berkeley, California 94720, United States; [orcid.org/0000-0001-7118-3228](https://orcid.org/0000-0001-7118-3228); Email: [ggu@berkeley.edu](mailto:ggu@berkeley.edu)

##### Authors

Zeqing Jin – Department of Mechanical Engineering,  
University of California, Berkeley, California 94720, United States

Zhizhou Zhang – Department of Mechanical Engineering,  
University of California, Berkeley, California 94720, United States

Xianlin Shao – Department of Mechanical Engineering,  
University of California, Berkeley, California 94720, United States

Complete contact information is available at:

<https://pubs.acs.org/10.1021/acsbmaterials.0c01761>

##### Notes

The authors declare no competing financial interest.

#### ACKNOWLEDGMENTS

The authors acknowledge support from Johnson & Johnson, Hellman Fellows Program, and 3M. Additionally, the authors would like to acknowledge Yifei Zhang and Zilan Zhang for their insightful discussions.

#### REFERENCES

- (1) Liu, R.; Wang, Z.; Sparks, T.; Liou, F.; Newkirk, J. 13 - Aerospace applications of laser additive manufacturing. In *Laser Additive Manufacturing*; Brandt, M., Ed.; Woodhead Publishing: 2017; pp 351–371, DOI: [10.1016/B978-0-08-100433-3.00013-0](https://doi.org/10.1016/B978-0-08-100433-3.00013-0).
- (2) Mota, C.; Puppi, D.; Chiellini, F.; Chiellini, E. Additive manufacturing techniques for the production of tissue engineering constructs. *J. Tissue Eng. Regen. Med.* **2015**, *9* (3), 174–190.
- (3) Gu, G. X.; Takaffoli, M.; Buehler, M. J. Hierarchically enhanced impact resistance of bioinspired composites. *Adv. Mater.* **2017**, *29* (28), 1700060.

- (4) Goh, G. D.; Agarwala, S.; Goh, G. L.; Dikshit, V.; Sing, S. L.; Yeong, W. Y. Additive manufacturing in unmanned aerial vehicles (UAVs): Challenges and potential. *Aerosp. Sci. Technol.* **2017**, *63*, 140–151.
- (5) Zhang, Z.; Demir, K. G.; Gu, G. X. Developments in 4D-printing: a review on current smart materials, technologies, and applications. *Int. J. Smart Nano Mater.* **2019**, *10*, 205.
- (6) Jin, Z.; Zhang, Z.; Demir, K.; Gu, G. X. Machine Learning for Advanced Additive Manufacturing. *Matter* **2020**, *3* (5), 1541–1556.
- (7) Mironov, V.; Boland, T.; Trusk, T.; Forgacs, G.; Markwald, R. R. Organ printing: computer-aided jet-based 3D tissue engineering. *Trends Biotechnol.* **2003**, *21* (4), 157–161.
- (8) Zhang, Y. S.; Yue, K.; Aleman, J.; Mollazadeh-Moghaddam, K.; Bakht, S. M.; Yang, J.; Jia, W.; Dell'Erba, V.; Assawes, P.; Shin, S. R.; Dokmeci, M. R.; Oklu, R.; Khademhosseini, A. 3D Bioprinting for Tissue and Organ Fabrication. *Ann. Biomed. Eng.* **2017**, *45* (1), 148–163.
- (9) Liu, X.; Yuk, H.; Lin, S.; Parada, G. A.; Tang, T. C.; Tham, E.; de la Fuente-Nunez, C.; Lu, T. K.; Zhao, X. 3D printing of living responsive materials and devices. *Adv. Mater.* **2018**, *30* (4), 1704821.
- (10) Barry, R. A., III; Shepherd, R. F.; Hanson, J. N.; Nuzzo, R. G.; Wiltzius, P.; Lewis, J. A. Direct-Write Assembly of 3D Hydrogel Scaffolds for Guided Cell Growth. *Adv. Mater.* **2009**, *21* (23), 2407–2410.
- (11) You, F.; Wu, X.; Chen, X. 3D printing of porous alginate/gelatin hydrogel scaffolds and their mechanical property characterization. *Int. J. Polym. Mater.* **2017**, *66* (6), 299–306.
- (12) Webb, B.; Doyle, B. J. Parameter optimization for 3D bioprinting of hydrogels. *Bioprinting* **2017**, *8*, 8–12.
- (13) Ribeiro, A.; Blokzijl, M. M.; Levato, R.; Visser, C. W.; Castilho, M.; Hennink, W. E.; Vermonden, T.; Malda, J. Assessing bioink shape fidelity to aid material development in 3D bioprinting. *Biofabrication* **2018**, *10* (1), No. 014102.
- (14) He, Y.; Yang, F.; Zhao, H.; Gao, Q.; Xia, B.; Fu, J. Research on the printability of hydrogels in 3D bioprinting. *Sci. Rep.* **2016**, *6* (1), 29977.
- (15) Naghieh, S.; Sarker, M.; Sharma, N.; Barhoumi, Z.; Chen, X. Printability of 3D printed hydrogel scaffolds: Influence of hydrogel composition and printing parameters. *Appl. Sci.* **2020**, *10* (1), 292.
- (16) Das, S.; Basu, B. An Overview of Hydrogel-Based Bioinks for 3D Bioprinting of Soft Tissues. *J. Indian Inst. Sci.* **2019**, *99* (3), 405–428.
- (17) Zhang, Z.; Jin, Y.; Yin, J.; Xu, C.; Xiong, R.; Christensen, K.; Ringeisen, B. R.; Chrisey, D. B.; Huang, Y. Evaluation of bioink printability for bioprinting applications. *Appl. Phys. Rev.* **2018**, *5* (4), No. 041304.
- (18) Chen, C. T.; Gu, G. X. Generative Deep Neural Networks for Inverse Materials Design Using Backpropagation and Active Learning. *Advanced Science* **2020**, *7*, 1902607.
- (19) Begg, R.; Kamruzzaman, J. A machine learning approach for automated recognition of movement patterns using basic, kinetic and kinematic gait data. *J. Biomech.* **2005**, *38* (3), 401–408.
- (20) Gu, G. X.; Chen, C.-T.; Buehler, M. J. De novo composite design based on machine learning algorithm. *Extreme Mechanics Letters* **2018**, *18*, 19–28.
- (21) Gobert, C.; Reutzel, E. W.; Petrich, J.; Nassar, A. R.; Phoha, S. Application of supervised machine learning for defect detection during metallic powder bed fusion additive manufacturing using high resolution imaging. *Additive Manufacturing* **2018**, *21*, 517–528.
- (22) Jin, Z.; Zhang, Z.; Ott, J.; Gu, G. X. Precise localization and semantic segmentation detection of printing conditions in fused filament fabrication technologies using machine learning. *Additive Manufacturing* **2021**, *37*, 101696.
- (23) Hanakata, P. Z.; Cubuk, E. D.; Campbell, D. K.; Park, H. S. Accelerated search and design of stretchable graphene kirigami using machine learning. *Phys. Rev. Lett.* **2018**, *121* (25), 255304.
- (24) Jin, Z.; Zhang, Z.; Gu, G. X. Automated Real-Time Detection and Prediction of Interlayer Imperfections in Additive Manufacturing

Processes Using Artificial Intelligence. *Advanced Intelligent Systems* **2020**, *2* (1), 1900130.

(25) Kim, S. H.; Lim, T. H.; Park, C. H. Silk Fibroin Bioinks for Digital Light Processing (DLP) 3D Bioprinting. In *Bioinspired Biomaterials*; Springer: 2020; pp 53–66, DOI: [10.1007/978-981-15-3258-0\\_4](https://doi.org/10.1007/978-981-15-3258-0_4).

(26) Alonzo, M.; Dominguez, E.; Alvarez-Primo, F.; Quinonez, A.; Munoz, E.; Puebla, J.; Barron, A.; Aguirre, L.; Vargas, A.; Ramirez, J. M.; Joddar, B. A comparative study in the printability of a bioink and 3D models across two bioprinting platforms. *Mater. Lett.* **2020**, *264*, 127382.

(27) Dalal, N.; Triggs, B. Histograms of oriented gradients for human detection. In *2005 IEEE computer society conference on computer vision and pattern recognition (CVPR'05)*; IEEE: 2005; pp 886–893, DOI: [10.1109/CVPR.2005.177](https://doi.org/10.1109/CVPR.2005.177).

(28) Zhou, B.; Lapedriza, A.; Khosla, A.; Oliva, A.; Torralba, A. Places: A 10 million image database for scene recognition. *IEEE Pami.* **2018**, *40* (6), 1452–1464.

(29) Xie, S.; Girshick, R.; Dollár, P.; Tu, Z.; He, K. Aggregated residual transformations for deep neural networks. In *Proceedings of the IEEE conference on computer vision and pattern recognition*; 2017; pp 1492–1500, DOI: [10.1109/CVPR.2017.634](https://doi.org/10.1109/CVPR.2017.634).

(30) Deng, J.; Dong, W.; Socher, R.; Li, L.-J.; Li, K.; Fei-Fei, L. Imagenet: A large-scale hierarchical image database. In *2009 IEEE conference on computer vision and pattern recognition*; IEEE: 2009; 248–255, DOI: [10.1109/CVPR.2009.5206848](https://doi.org/10.1109/CVPR.2009.5206848).

(31) Huh, M.; Agrawal, P.; Efros, A. A. What makes ImageNet good for transfer learning? *arXiv preprint arXiv:1608.08614*. 2016, <https://arxiv.org/abs/1608.08614> (accessed 2021-04-19).

(32) Kingma, D. P.; Ba, J. Adam: A method for stochastic optimization. *arXiv preprint arXiv:1412.6980*. 2014, <https://arxiv.org/abs/1412.6980> (accessed 2021-04-19).

(33) Ruder, S. An overview of multi-task learning in deep neural networks. *arXiv preprint arXiv:1706.05098*. 2017, <https://arxiv.org/abs/1706.05098> (accessed 2021-04-19).

(34) Ketkar, N. Introduction to pytorch. In *Deep learning with python*; Springer: 2017; pp 195–208, DOI: [10.1007/978-1-4842-2766-4\\_12](https://doi.org/10.1007/978-1-4842-2766-4_12)

(35) Adi, Y.; Nemcovsky, Y.; Schwing, A.; Hazan, T. On the generalization of bayesian deep nets for multi-class classification. *arXiv preprint arXiv:2002.09866*. 2020, <https://arxiv.org/abs/2002.09866> (accessed 2021-04-19).